

LA-UR-11-05295

Approved for public release;
distribution is unlimited.

Title: Three-dimensional constraint effects on the slitting method
for measuring residual stress

Author(s): C. C. Aydiner, Bogazici University
M. B. Prime, W-13, Los Alamos National Laboratory

Intended for: Journal of Engineering Materials and Technology, 2013, Vol.
135, pp. 031006-031001. DOI: 10.1115/1.4023849



Los Alamos National Laboratory, an affirmative action/equal opportunity employer, is operated by the Los Alamos National Security, LLC for the National Nuclear Security Administration of the U.S. Department of Energy under contract DE-AC52-06NA25396. By acceptance of this article, the publisher recognizes that the U.S. Government retains a nonexclusive, royalty-free license to publish or reproduce the published form of this contribution, or to allow others to do so, for U.S. Government purposes. Los Alamos National Laboratory requests that the publisher identify this article as work performed under the auspices of the U.S. Department of Energy. Los Alamos National Laboratory strongly supports academic freedom and a researcher's right to publish; as an institution, however, the Laboratory does not endorse the viewpoint of a publication or guarantee its technical correctness.

Three-dimensional Constraint Effects on the Slitting Method for Measuring Residual Stress

C. Can Aydiner

Assistant Professor

Department of Mechanical Engineering

Bogazici University

Bebek Istanbul 34342, Turkey

Email: can.aydiner@boun.edu.tr

Michael B. Prime

R&D Engineer

ASME Fellow

Los Alamos National Laboratory

Los Alamos, NM 87545

Email: prime@lanl.gov

ABSTRACT

The incremental slitting or crack compliance method determines a residual stress profile from strain measurements taken as a slit is incrementally extended into the material. To date, the inverse calculation of residual stress from strain data conveniently adopts a two-dimensional (2-D), plane strain approximation for the calibration coefficients. This study provides the first characterization of the errors caused by the 2-D approximation, which is a concern since inverse analyses tend to magnify such errors. 3-D finite element calculations are used to study the effect of the out-of-plane dimension through a large scale parametric study over the sample width, Poisson's ratio and strain gage width. Energy and strain response to point loads at every slit depth is calculated giving pointwise measures of the out-of-plane constraint level (the scale between plane strain and plane stress). It is shown that the pointwise level of constraint varies with slit depth, a factor that makes the effective constraint a function of the residual stress to be measured. Using a series expansion inverse solution, the 3-D simulated data of a representative set of residual stress profiles are reduced with 2-D calibration coefficients to yield the error in stress. The sample width below which it is better to use plane stress compliances than plane strain is shown to be about 0.7 times the sample thickness; however, even using the better approximation, the rms stress errors sometimes still exceed 3% with peak errors exceeding 6% for Poisson's ratio 0.3, and errors increase sharply for larger Poisson's ratios. The error is significant, yet, error magnification from the inverse analysis in this case is mild compared to, e.g., plasticity based errors. Finally, a scalar correction (effective constraint) over the plane-strain coefficients is derived to minimize the root-mean-square (rms) stress error. Using the posed scalar correction, the error can be further cut in half for all widths and Poisson's ratios.

Nomenclature

L, B, t	sample length, width, thickness
w	slit width
l_z, l_y	gage width and length
x	coordinate along slit extension
a	slit depth
P^i	stress series i th member
\mathbf{P}	stress series matrix
C^i	compliance series i th member
\mathbf{C}	compliance matrix
A_i	stress series coefficient i
U	total elastic energy per unit width
K_I	stress intensity factor
G	strain response to point/line load
E	Young's modulus
ν	Poisson's ratio
δ	point/line load at the slit face
Γ	effective level of constraint
γ	pointwise level of constraint
$2\varepsilon, 2\sigma$	subscript for plane strain, plane stress
3	subscript indicating three-dimensional analysis
\mathbf{In}	Penrose pseudo-inverse operator
\mathbf{R}	strain to stress reduction operator

1 Introduction

The slitting method (a.k.a. the crack compliance method) for measuring residual stress has found widespread application in the engineering community [1]. In this method, a narrow slit is incrementally extended into the sample and strain at strategic location(s) is measured at each step. This strain is due to the relaxation of residual stresses on the cut surface, and the original stresses can then be computed from the measured strain data - the inverse problem. The high strain signal inherent in the method as well as the well-conditioned nature of the inverse problem lead to its greatest benefit: measurement of through-thickness stress profiles with excellent spatial resolution and precision. The capability to resolve very low magnitude (around 10 MPa) residual stress profiles is indicative of the method's sensitivity [2].

In parallel to the method being applied to a broad range of materials and at various length scales [3–7], a series of studies have also targeted the method itself and its error sources. These studies were primarily motivated by the need to quantify systematic errors as part of writing an international standard for the slitting method. The studies have been designed to isolate each error source in turn after some preliminary studies showed that each error source could be reasonably decoupled from the others so long as the studies were consistent in the geometry studied.

As far as error sources, there is the problem of how the inherent uncertainty in the measured strains translates to the calculated stresses through the inverse problem [8]. Secondly, systematic errors are introduced into the computed stresses from any discrepancies between the exact experimental details and how these are modeled to solve the inverse problem. The model-experiment discrepancy can be geometrical such as differences in the domain size, slit width, and the length of the strain gage (the latter's effect on the slitting measurement is studied by Lee and Hill [9]). Furthermore, the validity level of typical simplifying assumptions of the model is in question. Major assumptions of this kind are: (i) The material remains linear elastic during material removal. (ii) The finite width of the slit can be ignored (assuming a perfect crack). (iii) The model domain can be considered to be two-dimensional (2-D) with the plane-strain (pl- ϵ) assumption.

Prime [10] recently studied the assumption that the stresses relax elastically and laid out the limiting magnitude and profile of residual stresses that would cause errors from plasticity. That study investigated a perfectly plastic material under plane stress (pl- σ) and pl- ϵ assumptions as well as a limited number of intermediate three-dimensional (3-D) cases since plastic behavior strongly depends on the out-of-plane constraint level.

This work, in turn, studies assumption (iii) of approximating a 3-D experiment with a 2-D model. For material with a Poisson's ratio near 0.3, the difference between pl- σ and pl- ϵ would only be about 10% in the forward problem: strain for a given stress. However, determining stresses from strains through the inverse problem might well amplify such errors.

The study entails technical difficulty because of need for 3-D calculations over wide ranges of multiple independent variables. The difficulty might explain why such work has been lacking in literature. Because of the wide usage of 2-D approximations, the basic issue investigated here is what *effective* out-of-plane constraint level (between pl- σ and pl- ϵ) should be used in standard models based on 2-D calculations. Although, this is a rather obvious parameter to seek, related method literature is scarce and does not address the question directly. Cheng and Finnie [11] described a simple method to obtain effective stress intensity factors (SIF) in a 3-D problem inspired from the formulation of the slitting method. In the most relevant work, Nervi and Szabo [12] laid out a 3-D analysis methodology but only gave results specific to one application. Fratini and Pasta [13] also used a 3-D analysis specific to one application.

In likeness to all aforementioned slitting method investigations as well as the overwhelming majority of experimental studies that utilize the method, the *rectangular bar* sample geometry is considered. Here, three-dimensional model domains are examined in an extensive and systematic parametric study

over the sample width (the primary variable), Poisson's ratio and strain gage width. Scripting and database utilization are employed to process and manage the finite element analysis (FEA).

2 Methods

2.1 Method basics and the parameter space

Fig. 1 shows the slitting terminology and the sample geometry. To save space, the figure also depicts the considered (a) 2-D and (b) 3-D FEA domains. The full sample of length L , width B , and thickness t

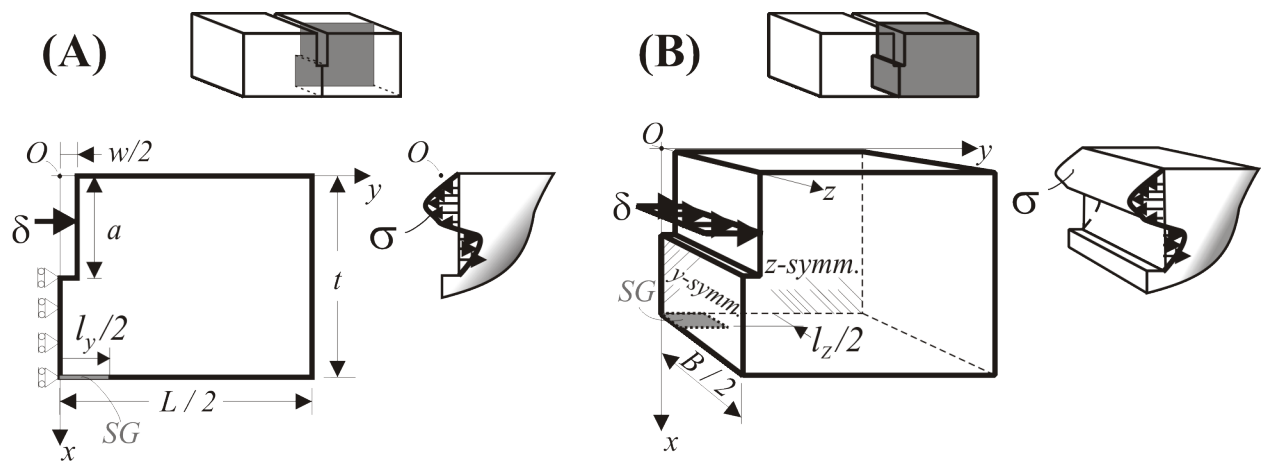


Fig. 1. The (a) 2-D and (b) 3-D finite element domains of the slitting sample depicted as shaded regions in the top sketches of the entire sample. O is the origin of the chosen x - y - z coordinate system; SG stands for strain gage; δ is a point/line load in (a)/(b).

is depicted in the sketches on the top in which shaded regions correspond to the FEA domains. In this study, all dimension/coordinate values are to be understood to be normalized by t . Hence, thickness itself gets fixed at 1; x -coordinate ranges from 0 to 1 (from the origin, O , at the top of the sample to its bottom); and, e.g., $B = 2$ corresponds to a sample width that is twice the thickness. The slit depth and width are denoted by a and w , respectively. The slitting plane is symmetrically located in the sample leaving half the sample length on each side. A single strain gage (gage length l_y and width l_z) is located at the center of the bottom face to measure the y -component of normal strain as the cut depth a is incrementally extended. Strain data, denoted by ϵ_i , is recorded at n depths (typically, $n \sim 40$):

$$\epsilon_y(a_i) = \epsilon_i, \quad i = 1, \dots, n. \quad (1)$$

The entire set of strain data and measurement depths are represented by $\{\varepsilon\}$ and $\{a\}$, respectively. The shown strain gage placement is optimal for determining through-the-thickness stress profiles [1], $\{\sigma_y\}$, through an inverse solution, which is represented here by the operator \mathbf{R} . From here on, the subscript y is dropped for simplicity, since no stress/strain component other than the normal y -component will be considered. Then,

$$\{\sigma\} = \mathbf{R}(\{\varepsilon\}, \mathbf{p}) \quad (2)$$

where \mathbf{p} stands for “parameters”.

Given the large number of parameters in the three-dimensional slitting problem, constraining the parameter space—fixing certain variables at their typical values—is necessary to keep the study manageable. Here the parameters with the least effect on 3D constraint are fixed to values consistent with previous work so that the results of this study can be used in conjunction with those studies. Accordingly, since Lee and Hill [9] provide a parametric study over l_y in the two-dimensional framework, l_y will be fixed to the central value $l_y = 0.07$ about which they offer corrections. Similarly, consistent with [9], sample length here is fixed^a to its typical value $L = 4$.

The parameter set of this 3-D investigation, defined as $\mathbf{p}_3 = \{L, B, w, l_y, l_z, \nu\}$, is listed in the first column of Table I). The part of this set that applies to the 2-D problem is $\mathbf{p}_2 = \{L, w, l_y\}$. All parameters are assigned a “norm” value in the second column of Table I. The third column shows the parameters that will be varied in the study and their ranges. The primary variable is the width of the sample which will be allowed to vary in the interval [0.2,2]. In addition, the effect of varying the Poisson’s ratio ν and l_z are considered. The study only considers a perfect crack slit, $w = 0$, for several reasons. First, the slit width has some effect on the measured strains and on constraint at the crack tip, but negligible effect on the issue this study is trying to isolate: the 3D/pl- σ /pl- ε effects on strains measured at the back face strain gage [14]. Furthermore, studying the perfect crack retains consistency with previous method work [9, 10] and allows the utilization of energy-based fracture mechanics concepts that the slitting method formulation historically utilized [1].

^aAccommodating this precise L is often possible since the sample is usually cut out from larger plates. This operation is also related to how $L = 4$ is picked; it is a length sufficiently large for $\sigma_y(x)$ in the original plate to be predominantly preserved in the experimental sample.

parameter	norm value	considered values
length (L)	4	fixed
width (B)	1	0.2, 0.3, ..., 2
Slit width (w)	0	fixed
Gage length (l_y)	0.07	fixed
Gage width (l_z)	0	0, 0.04, ..., 0.2
Poisson's ratio (ν)	0.3	0.2, 0.25, ..., 0.4

Table I. Parameters (\mathbf{p}_3) of the study (column 1), their norm values (column 2), and considered values/ranges of the parametric study (column 3).

In Table I, Young's modulus is not listed as a parameter since it trivially scales with the solution

$$\{\sigma\} = \mathbf{R}(\{\varepsilon\}, E, \dots) = E \cdot \mathbf{R}(\{\varepsilon\}, \dots) \quad (3)$$

in this linear elasticity problem with only traction boundary conditions. Only in 2-D, a trivial normalization like this is possible for Poisson's ratio as well :

$$\{\sigma\} = E'_{\bullet} \cdot \mathbf{R}(\{\varepsilon\}, \mathbf{p}_2) \text{ where } E'_{2\varepsilon} = \frac{E}{1-\nu^2}, E'_{2\sigma} = E \quad (4)$$

where \bullet can stand for 2ε and 2σ , indicating pl- ε and pl- σ assumptions, respectively^b. Hence, \mathbf{p}_2 excludes ν that remains a parameter in the 3-D case.

2.2 The Green's function formulation

The gage response of the 2-D and 3-D domains are investigated with a Green's function formulation, which gives the greatest flexibility for applying the results to different inverse solutions and for physically interpreting the results. In Fig. 1(a), the point load δ applied at coordinate x when the slit depth is a will be denoted $\delta_{2\varepsilon}(x, a)$ for pl- ε and $\delta_{2\sigma}(x, a)$ for pl- σ . For the 3-D domain [Fig. 1(b)], the point load is replaced with a uniform line load at constant x , denoted $\delta_3(x, a)$ that has a unit resultant. The strain response to δ at the strain gage is denoted with G . The G notation will correspond to the introduced δ

^bEq. 4 applies rigorously for linear elastic fracture mechanics conditions.

notation to signify the specific problem:

$$\begin{aligned}\delta_{2\varepsilon}(x, a) &\Rightarrow G_{2\varepsilon}(x, a, \mathbf{p}_2) \\ \delta_3(x, a) &\Rightarrow G_3(x, a, \mathbf{p}_3)\end{aligned}\quad (5)$$

where the parameter dependence of the strain responses is specifically indicated.

Given the residual stress profile $\sigma(x)$, $0 \leq x \leq 1$ (tensile positive), the cropped domains in Fig. 1 on the right of each FEA domain show equal-valued traction profiles applied on the slit surface of stress-free domains. From Bueckner's principle, this surface traction produces the same deformation that is due to the relaxation of residual stress, with the implied superposition valid only with linear elasticity [1, 10, 15].

Utilizing the illustration in Fig. 1(b), an *inherent* assumption of the incremental slitting method is brought up at this point: $\sigma(x)$ is assumed constant along the transverse (z) direction, which justifies the use of line loads, $\delta_3(x, a)$, in constructing the strain response of an arbitrary $\sigma(x)$.

Using the flexibility of the Green's function approach, the strain response at the strain gage to an arbitrary stress profile, $\sigma(x)$ is given by

$$\varepsilon_{\bullet}(a, \mathbf{p}_{\bullet}) = \int_0^a \sigma(x) G_{\bullet}(x, a, \mathbf{p}_{\bullet}) dx, \quad (\bullet) = 2\varepsilon, 2\sigma, 3 \quad (6)$$

as a function of slit depth and parameters. The \bullet has been introduced as a placeholder for 2ε , 2σ , or 3 . For \mathbf{p}_{\bullet} , both 2ε and 2σ as subscript will mean \mathbf{p}_2 .

2.3 The inverse problem

In accordance with [9, 10] and the majority of the incremental slitting method literature, the stress-series based inverse solution method will be investigated here (for other approaches, see e.g., [16]). In this method, residual stress is assumed to be a linear combination of a function series, P^j ,

$$\sigma(x) = \sum_{j=1}^m A_j P^j(x) \quad (7)$$

where m is the fit order and A_j are the scalar weights. Due to their orthonormality and automatic satisfaction of equilibrium [1, 10], the series is chosen as Legendre polynomials starting from order 2. Thus, $P^j = \text{Leg}^{j+1}$. The first four stress functions are shown in Fig. 2(a). The maximum order that will be considered here is $m = 11$. Higher fit orders are rarely useful due to the deteriorating condition of the inversion with increasing fit order. The strain that would be observed at the strain gage if the residual stress, $\sigma(x)$, was equal to $P^j(x)$ is called the compliance C^j . Using Eq. 6,

$$C_{\bullet}^j(a, \mathbf{p}_{\bullet}) = \int_0^a P^j(x) G_{\bullet}(x, a, \mathbf{p}_{\bullet}) dx, \quad (\bullet) = 2\varepsilon, 2\sigma, 3. \quad (8)$$

Recalling Eq. 1 (n data points at discrete depths), measured strain is given by

$$\varepsilon_i \approx \sum_{j=1}^m A_j C_{\bullet}^j(a_i, \mathbf{p}_{\bullet}), \quad i = 1, \dots, n \quad (9)$$

in direct correspondence to Eq. 7 because of linear superposition. Here, ‘ \approx ’ implies that experimental data is not, in general, reproduced exactly by the least squares fit. In the following matrix equations, vectors in curly brackets ($\{\}$) indicate column vectors. With $n > m$, the least-squares best approximation for the m coefficients $\{A\}$ is in the Moore-Penrose pseudoinverse form:

$$\{A\} = (\mathbf{C}_{\bullet}^T \mathbf{C}_{\bullet})^{-1} \mathbf{C}_{\bullet}^T \{\varepsilon\} = \mathbf{In}_{\bullet} \cdot \{\varepsilon\}, \quad (\bullet) = 2\varepsilon, 2\sigma, 3 \quad (10)$$

where \mathbf{C}_{\bullet} is the $n \times m$ compliance matrix whose row i -column j member is $C_{\bullet}^j(a_i, \mathbf{p}_{\bullet})$. Let us also define \mathbf{P} as the corresponding stress series matrix with components $P^j(a_i)$. The second equality in Eq. 10 serves to shorthand the pseudoinverse with \mathbf{In}_{\bullet} . So, the inverse solution for stress (at $x = a_i$ points) is found by inserting Eq. 10 in Eq. 7:

$$\{\sigma_{\bullet}\} = \mathbf{P} \cdot \mathbf{In}_{\bullet} \cdot \{\varepsilon\} = \mathbf{R}_{\bullet} \cdot \{\varepsilon\}, \quad (\bullet) = 2\varepsilon, 2\sigma, 3 \quad (11)$$

where the second equation defines the inverse solution operator (originally introduced in Eq. 2) as the linear operator \mathbf{R}_{\bullet} . The parameter dependencies, which are not specified in the above equations to avoid

overcrowding the expressions, are given by

$$\{\sigma_{\bullet}\} = \{\sigma_{\bullet}(\mathbf{p}_{\bullet}, m)\} \quad ; \quad \mathbf{R}_{\bullet} = \mathbf{R}_{\bullet}(\mathbf{p}_{\bullet}, m) \quad ; \quad \mathbf{In}_{\bullet} = \mathbf{In}_{\bullet}(\mathbf{p}_{\bullet}, m) \quad (12)$$

where fit order m is signified as the additional parameter that comes from the inverse solution procedure. The result $\{\sigma_{\bullet}\}$ has substantial dependence on m , whose optimal selection is a complex problem [8].

Since computational data is generated in this study, there will be no measurement errors in the considered $\{\varepsilon\}$. However, the inverse solution (Eq. 11) will have some dependence on the specific data depths ($\{a\}$). To limit complexity, the data depths will be fixed to a finely-spaced, uniform-interval set $a = 0.02, 0.04, \dots, 0.92$. Here, 0.92 is chosen to represent the typical maximum experimental data depth.

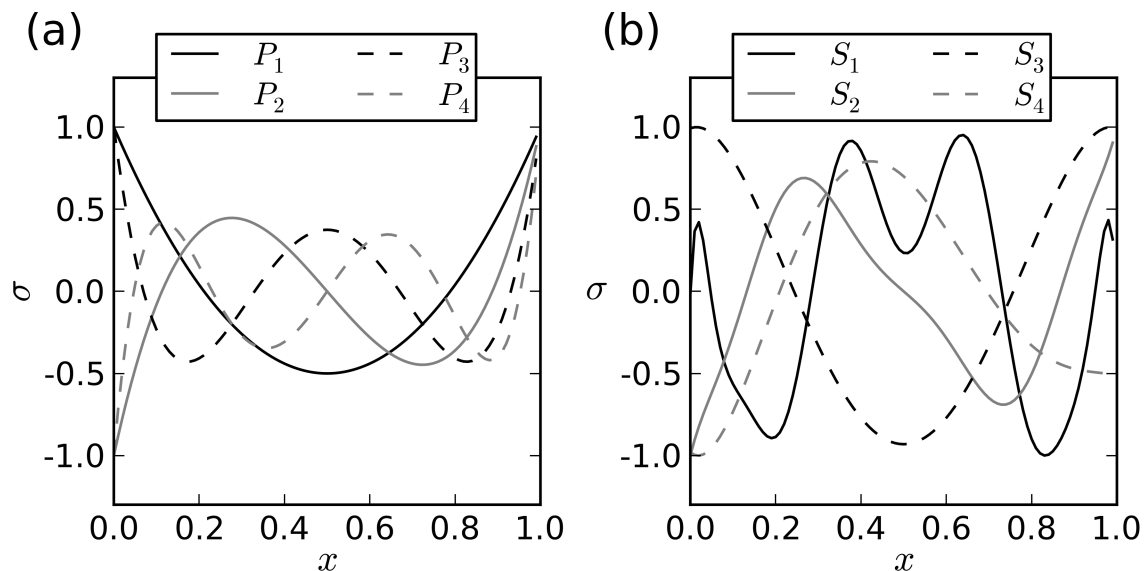


Fig. 2. (a) The first four elements of the stress series (Legendre polynomials 2 to 5), (b) the considered residual stress profiles detailed in Table II.

2.4 The error formulation

In order to compare stress profiles calculated with different approximations, error measured must be defined. Given two equal-length vectors $\{v\}$ and $\{w\}$, the error vector, $\text{err}(v, w)$, is defined here as

$$\text{err}(v, w) = \frac{\{v\} - \{w\}}{\max(|\{w\}|)} \quad (13)$$

Name	Cause	Order (m^*)	Nonzero A_i
S_1	rolling	11	$A_1=-0.685$, $A_2=-0.056$, $A_3=1.392$, $A_4=0.104$, $A_5=0.223$, $A_6=0.008$, $A_7=-$ 1.028 , $A_8=-0.214$, $A_9=0.602$, $A_{10}=0.095$, $A_{11}=-0.582$
S_2	plastic bending	10	$A_2=1.259$, $A_4=-0.193$, $A_6=-0.242$, $A_8=0.208$, $A_{10}=-0.032$
S_3	quenching [10]	3	$A_1=1.489$, $A_3=-0.496$
S_4	plastic compression on top surface [8]	4	$A_1=-1.12$, $A_2=0.467$, $A_3=0.373$, $A_4=-0.233$

Table II. Considered residual stress profiles, their typical causes, Legendre series order (m^*) and coefficients (A_i).

2.5 Specifics of the finite element analysis

In order to handle the large parameter space, the Abaqus[©] [17] software employed for FEA is encompassed by a software structure coded in pythonTM [18] further using scientific tool packages such as SciPy [19]. There are two distinct stages of the process: (i) the automation of FEA computations for a desired parameter space, (ii) processing the desired subset of computational data (“slitting reduction”). These stages communicate with a common database which is filled with the targeted parameter space at the start of the operation. Once the database is formed/appended, each unprocessed line is executed successively through the three stages of the FEA analysis: (i) formation of the model (script fed to Abaqus Scripting Interface), (ii) execution (Abaqus Standard), (iii) postprocessing [retrieving displacement and energy data and storing them (script fed to Abaqus Scripting Interface)]. In the ”data” reduction stage that follows calculations, the database is consulted to locate the displacement/energy output files for a desired subset of the parameter space. Then, the gage strain is computed from displacement data in accordance with the gage dimension specification (l_y , l_z). With this raw result, further utilities implement all equations/evaluations in the text.

The 3-D meshing scheme is illustrated in Fig. 3 for norm parameters. The meshing scheme involves a regular mesh of hexahedron elements followed by a coarsening mesh of wedge elements. The hexahedron region provides high resolution next to the loading surface with 100 quadratic, reduced integration, C3D20R elements spanning the thickness of the sample. The C3D15 wedge elements have the same interpolation order. The length of the wedges/hexahedrons in the z-direction is kept uniform all through the mesh. The corresponding 2-D mesh—whose results are to be compared to the shown mesh (Eq. 16)—is a slice of the 3-D mesh in any $x - y$ plane (say, the front face). The 2-D elements

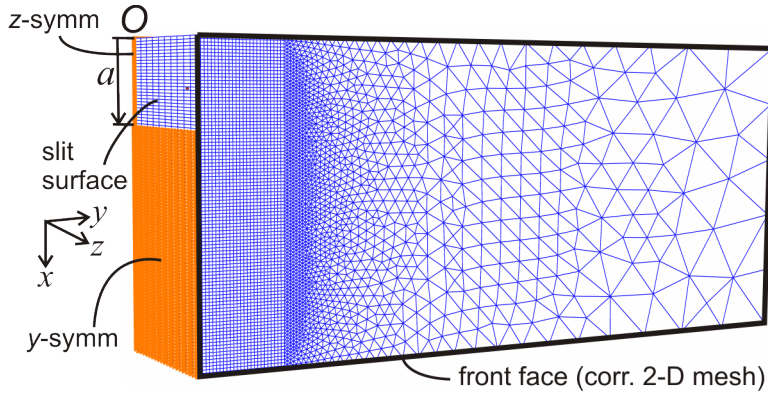


Fig. 3. A considered 3-D finite element mesh composed of wedge and hexahedron elements. All parameters are at norm values ($B = 1$, $L = 4$, $w = 0$) and the shown slit depth, a , is arbitrary. O is the origin (refer to Fig. 1(b) for notation) and the front face is placed in a rectangle also revealing the corresponding 2-D mesh. The x-y-z triad is displaced from O for clarity.

are chosen with the same interpolation order: CPE8R/CPS8R rectangle and CPE6/CPS6 triangle for pl- ϵ /pl- σ . Using *matching* meshes, the finite element discretization error is kept at the same order to cancel in the comparison (Eq. 16). This argument, however, holds strictly only in the $x - y$ plane and the number of elements in the z -direction (n_z) is checked for convergence for 3-D models: Comparing $n_z = 5$ and $n_z = 10$ analyses, the former demonstrates sufficient convergence for all widths. Given a set of parameters, $n = 46$ finite element analyses are submitted to Abaqus Standard, one for each depth, $a_i = 0.02i$, $i = 1, \dots, 46$. In each run, $\delta_{\bullet}(x, a_i)$ is applied at all x values that fall on mid-nodes and element boundaries, namely, at $x = J \cdot 0.005$ with $x < a_i$, J positive integer. This results in $4 * i$ load cases for each analysis i , and for the last ($i = 46$, $a = 0.92$) analysis, the number of analyzed loads climb to 184. Consequently, through the 46 runs, $2n(n + 1) = 4324$ (load point x , slit depth a) pairs are evaluated. In the Abaqus implementation, the *LOADCASE command is used for efficiency. Once the analysis is finished, corresponding $G_{\bullet}(x, a, \mathbf{p}_{\bullet})$ is evaluated ("Slitting reduction" stage) at the 4324 points of the (x, a) mesh. Evaluation of Eqs. [6,8] is performed via numerical integration from these discrete points.

The total elastic energy of the domain is also stored at the (x, a) mesh defined above, obtained by summing the integrated elastic energy of all elements. To compare 2-D and 3-D cases, this energy needs to be normalized per width and the resulting quantity is denoted $U_{\bullet}(x, a, \mathbf{p}_{\bullet})$, $(\bullet) = 2\epsilon, 2\sigma, 3$.

3 Results and discussion

A slitting experiment is typically analyzed with the pl- ϵ compliance, such as those accurately available in [9]. Taking this compliance as a base, the natural task is to offer simple functional corrections on it to approximate the 3-D compliance for any \mathbf{p}_3 . Prompted by the straightforward conversion from pl- ϵ to pl- σ compliances, i.e., $\mathbf{C}_{2\sigma} = \Gamma \mathbf{C}_{2\epsilon}$ where $\Gamma = (1 - \nu^2)^{-1}$ (recall Eq. 4), the intuitive correc-

tion is multiplication by a factor: $\mathbf{C}_3(\mathbf{p}_3) \simeq \Gamma(\mathbf{p}_3) \mathbf{C}_{2\varepsilon}$. Here, one expects to find $\Gamma(\mathbf{p}_3)$ such that $1 < \Gamma < (1 - \nu^2)^{-1}$, where $\Gamma = 1$ and $\Gamma = (1 - \nu^2)^{-1}$ are the two extremes corresponding to pl- ε and pl- σ cases, respectively. The intermediate value $\Gamma(\mathbf{p}_3)$ will be called the “effective constraint”.

A clear-cut result would be obtained if the effective constraint just depends on the parameters \mathbf{p}_3 as conjectured. Section 3.1, however, presents and provides theoretical footing for the fact that it is also a function of the particular residual stress. This is the fundamental difficulty that surfaced in this work and is apparent in all the practical results presented in the later sections.

3.1 The slit depth dependence of the level of constraint

Before tackling the problem of the effective (average) Γ , first consider adjusting the pl- ε Green’s function by a pointwise definition of the level of constraint factor γ

$$G_{\bullet}(x, a, \mathbf{p}_{\bullet}) = \gamma(x, a, \mathbf{p}_{\bullet}) G_{2\varepsilon}(x, a, \mathbf{p}_2) \quad , \quad (\bullet) = 2\sigma, 3 \quad (17)$$

for it to match the pl- σ or the 3-D Green’s function. Naturally, if $(\bullet) = 3$, intersecting elements of \mathbf{p}_3 and \mathbf{p}_2 are taken equal in the above expression. Inserting Eq. 17 in Eq. 6 yields:

$$\varepsilon_{\bullet}(a, \mathbf{p}_{\bullet}) = \int_0^a \sigma(x) \gamma(x, a, \mathbf{p}_{\bullet}) G_{2\varepsilon}(x, a, \mathbf{p}_2) dx \quad , \quad (\bullet) = 2\sigma, 3 \quad (18)$$

For the case of pl- σ , $\gamma(x, a, p_2)$ remains constant at $(1 - \nu^2)^{-1}$, since Eq. 4 is valid for any symmetric mode-I loading including the application of individual δ -loads. This leads to the trivial equality of pointwise and effective constraints: $\gamma(x, a, p_2) = \Gamma = (1 - \nu^2)^{-1}$.

In contrast, if γ has (x, a) dependence, the effective constraint that will reflect in strain (Eq. 18) will be modulated by the particular stress $\sigma(x)$. This is indeed the case in 3-D, as demonstrated in Fig. 4(a) where γ is plotted vs. (x, a) for norm parameters ($B = 1$, $\nu = 0.3$). (For norm $\nu = 0.3$, $(1 - \nu^2)^{-1} = 1.099$.) Eq. 18 yields that (i) the effective constraint, Γ , for 3-D compliances will be a function of $\sigma(x)$, and (ii) this modulation will further be a function of depth (observe the ratio $\varepsilon_3/\varepsilon_{2\varepsilon}$ will vary with a). The latter complexity shows in the appropriate Γ definition (Section 3.4).

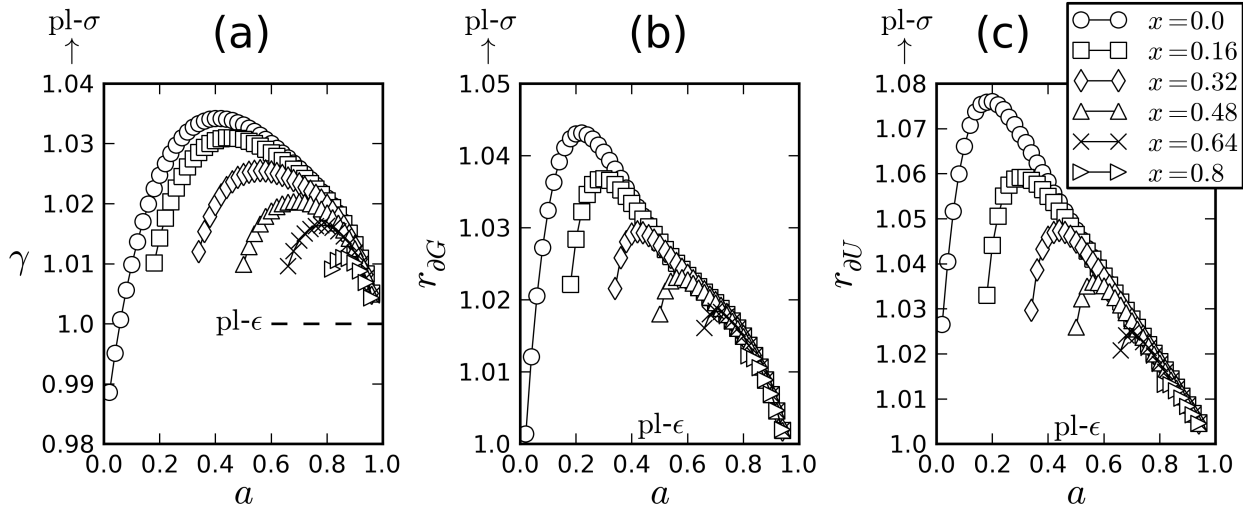


Fig. 4. For $B = 1$ and $\nu = 0.3$, constraint ratios (Eq. 19) of (a) strain at the gage, (b) depth-derivative of the strain at the gage, and (c) energy release rate. Each curve in parts (a), (b) or (c) corresponds to fixing the δ -load (see Fig. 1) at the x value shown in the legend and plots the corresponding ratio as a function slit depth a . The $\text{pl-}\sigma$ level is at $(1 - \nu^2)^{-1} = 1.099$.

3.2 Fracture mechanics interpretation

This section will discuss that the results of Fig. 4(a) do not correspond to available results in the crack-tip literature, and then attempt to provide fracture-mechanics based insight into the reasons for the particular constraint behavior observed. These discussions are not critical for readers only interested in the final outcome. Investigating the problem at this fundamental level, however, will also be crucial for future work in formulating corrections on inverse solution methods other than the stress-series based one studied in this paper.

Previous fracture mechanics results on constraint do not apply well to the current study. In the fracture mechanics literature on the 3-D edge-crack problem (e.g., [20–23]) the constraint level is presented in stress terms (as with $\sigma_z/\nu(\sigma_x + \sigma_y)$, called ‘degree of plane strain’). The focus there is to trace the constraint level (and plastic zones) along the crack tip as the condition goes from $\text{pl-}\epsilon$ in the mid-plane to $\text{pl-}\sigma$ on the surface. In the geometric setup of the problem, shallow or deep cracks are avoided and far field loading is applied. However, shallow and deep crack situations are a part of the physical problem in slitting measurements, as well as loads that are close enough to the crack tip to alter the crack-tip stress distributions. Furthermore, the constraint level of interest ($\gamma(x, a, \mathbf{p}_3)$) here is fundamentally different because it relates to strains measured away from the crack tip.

To help interpret the constraint behavior, Fig. 4 (a), (b), (c) plot γ , $r_{\partial G}$, and $r_{\partial U}$, respectively, with

their definitions given by

$$\gamma = \frac{G_3}{G_{2\varepsilon}} \quad ; \quad r_{\partial G} = \frac{\left(\frac{\partial G_3}{\partial a}\right)}{\left(\frac{\partial G_{2\varepsilon}}{\partial a}\right)} \quad ; \quad r_{\partial U} = \frac{\left(\frac{\partial U_3}{\partial a}\right)}{\left(\frac{\partial U_{2\varepsilon}}{\partial a}\right)} \quad . \quad (19)$$

These plots present the (x, a) dependence by plotting selected constant- x curves versus slit depth a . Physically, the $x = 0$ curve in Fig. 4(a) depicts fixing the δ -load at the top corner and plotting the ratio of 3-D and pl- ε responses at the strain gage as the slit (crack) is incrementally extended. In this way, the individual curves in Fig. 4(c) plot the ratio of "energy release rates"^c, $r_{\partial U}$ as the crack is extended, with δ -load fixed at x .

To show the role of $r_{\partial U}$ and $r_{\partial G}$ in the "level of constraint" discussion, firstly note

$$\frac{\partial U_{\bullet}}{\partial a} = \left(\frac{K_{I\delta}^2}{E}\right)_{\bullet} \quad , \quad (\bullet) = 2\varepsilon, 2\sigma, 3 \quad (20)$$

which gives the energy release rate when δ at x is the sole load on the body and $K_{I\delta}$ is its SIF. Secondly, Castigliano's theorem is recalled to link energy and deformation at the strain gage—a typical operation in the derivation of the fracture-mechanics-based compliances (see, e.g., [24]). For this, an imaginary force, F is applied in $+y$ direction at the end point of the gage [at coordinates $(1, l_y)/(1, l_y, 0)$ for the 2-D/3-D case] simultaneously with δ . The energy release rate under this loading is then given by

$$\frac{\partial U_{\bullet}}{\partial a} = \left[\frac{(K_{I\delta} + K_{IF})^2}{E}\right]_{\bullet} \quad , \quad (\bullet) = 2\varepsilon, 2\sigma, 3 \quad (21)$$

where K_{IF} is the SIF due to F . Carrying out the theorem (see, e.g., Schindler et al. [25] for details) yields

$$\frac{\partial G_{\bullet}}{\partial a} = \frac{1}{l_y} \left(\frac{K_{I\delta} K_{IF}}{E}\right)_{\bullet} \quad , \quad (\bullet) = 2\varepsilon, 2\sigma, 3. \quad (22)$$

^cFor the dead load problems in a linear elastic body, the elastic energy of the system (U defined in Section 2.5) is increased by the released amount during crack extension [15].

assuming *unit F*. Using Eqs. 20 and 22, and observing the equality of SIFs for pl- σ and pl- ϵ , the pl- σ to pl- ϵ ratios $(\partial U_{2\sigma}/\partial a)/(\partial U_{2\epsilon}/\partial a)$ and $(\partial G_{2\sigma}/\partial a)/(\partial G_{2\epsilon}/\partial a)$ once again yield $E_{2\epsilon}/E_{2\sigma} = (1 - \nu^2)^{-1}$, in likeness to γ and Γ . It follows that $r_{\partial G}$ and $r_{\partial U}$ of Eq. 19, which are the similar ratios between 3-D case and pl- ϵ , can be regarded as measures of the degree of constraint. The energy release rate ratio, $r_{\partial U}$ [see Fig. 4(c)], is an encompassing measure that is associated with the entire body—no dependence on a particular gage location. $r_{\partial G}$ plotted in Fig. 4(b), shows a similar trend to $r_{\partial U}$, but no exact numerical similarity. This is because $r_{\partial G}$ (and, naturally then, γ) depends on gage location in the 3-D domain. [To illustrate with an example: if the gage was taken as wide as the sample itself, the peak value of the $x = 0$ curve for γ (or $r_{\partial G}$) would increase to 1.048 (1.058) from its current 1.034 (1.043). The form of the curves (not shown) would also be somewhat altered.] To elaborate briefly, Eqs. 20-22 are in fact 2-D formulations and $(\bullet) = 3$ is allowed for a possible *effective* extension to 3-D. (If indeed pl- ϵ /pl- σ values of $K_{I\delta}$ and K_{IF} remained valid for 3-D, Eqs. 20 and 22 would lead to $r_{\partial U} = r_{\partial G} = E_{2\epsilon}/E_3$, where E_3 is an effective 3-D modulus.) As is well known, in the pl- ϵ /pl- σ cases, given any particular mode-I loading, the crack tip stresses have an invariant characteristic distribution that is merely amplified with K_I . This underlies the superposition $K_{IF} + K_{I\delta}$ in Eq. 21. For the 3-D domain, however, point force F at the mid-point of the bottom surface and δ uniform line load at the slit do not produce stress distributions of the same functional form, along the crack front in the z -direction. The ensuing invalidity of the superposition in Eq. 21 sheds light on the discrepancy of $r_{\partial U}$ and $r_{\partial G}$ from Castigliano's Theorem perspective.

For physical deductions, $r_{\partial U}$ is considered first, as the measure of the crack-tip constraint level. It is noticed in Fig. 4(c) that individual curves join, once the crack tip (a) moves sufficiently away from the load application points (x). (Whether δ -force is at $x=0$ or $x=0.16$, once the crack tip moves away from 0.16, the same crack-tip constraint level is observed.) This 'master' curve may roughly be defined as the linearly decreasing portion of the $x = 0$ curve.^d The primary deduction here is that the constraint level is near pl- σ at low depths (around $a = 0.2$, $r_{\partial U} \sim 1.08$ nearing the pl- σ value 1.099), and goes toward pl- ϵ as the crack-tip gets closer to the bottom face. This can be explained with the increased constraining effect of the bulk relative to the increased compliance of the ligament as it thins. Note also that, before each load-curve joins the master curve, i.e, for δ near a , $r_{\partial U}$ is more pl- ϵ than the master curve itself. This is likely a ramification of the stress field under the point load coupling with the crack-tip stress field.

$r_{\partial G}$ -curves are akin to $r_{\partial U}$ -curves with the existence of a master curve as well as the primary pl- σ to

^dIt is natural to ask whether the peak portion of the $x = 0$ curve is also characteristic. Looking at the results of immediate neighbor δ -loads at $x = 0.05, 0.01, \dots$, this part of the curve does not remain invariant, but drops steadily with increasing x .
MATS-12-1140, Aydiner, Page 16

pl- ϵ trend with increasing depth. γ curves of Fig. 4(a), on the other hand, do not exhibit a master curve and are more *average*: Note in this regard that γ can be obtained by placing an integral (over a) both to the numerator and denominator of $r_{\partial G}$ in Eq. 19. Hence, γ is not a ‘sharp’ measure over the crack-tip position, but regardless, it is the parameter that concerns this study (Eq. 17). Finally, Fig. 5 plots this parameter for different sample widths, when the δ -load is fixed to the top corner. Naturally, for smaller sample widths the curves tend to pl- σ and vice versa. However, the concave character of the curves is invariant.

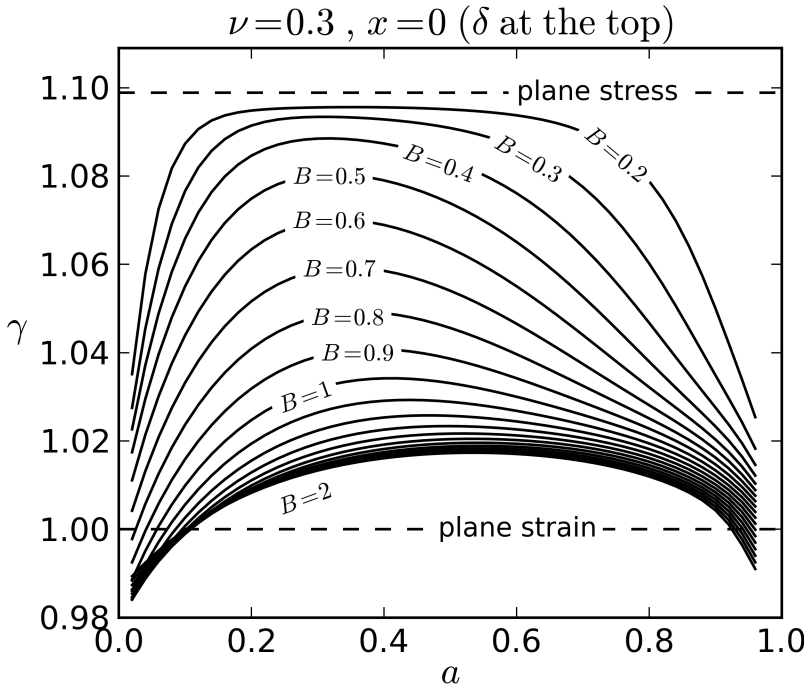


Fig. 5. The ratio of the measured strain, γ , in the 3-D analysis to plane strain analysis as a function of slit depth a . The particular loading is a δ -load (see Fig. 1) at the top ($x = 0$). This figure is at the norm point of the parameter space $\mathbf{v} = 0.3$, etc., except for each curve corresponding to different sample widths as indicated.

3.3 Plane stress versus plane strain

Before exploring any correction, this section will present the stress error level due to utilizing uncorrected 2-D compliances in the inverse problem as a function of sample width, B (all other parameters at norm values). In this discussion, it is important to consider that pl- σ compliance will bear less error than the pl- ϵ compliance for widths smaller than a certain value. This particular transition width has been another unanswered question for the user. The errors, a la Eq. 16, $e_{\text{rms}}(\sigma_{2\epsilon}, \sigma_3)$ and $e_{\text{rms}}(\sigma_{2\sigma}, \sigma_3)$ are plotted as a function of B in Fig. 6 with solid and hollow markers, respectively. Fig. 6(a) is reserved for selected members of the stress series whereas Fig. 6(b) depicts the stress cases of Table II. The in-

tersection of the pl- σ and pl- ϵ curves, shown with dashed lines for profile S_1 in Fig. 6(b) is the transition width (~ 0.63 for S_1).

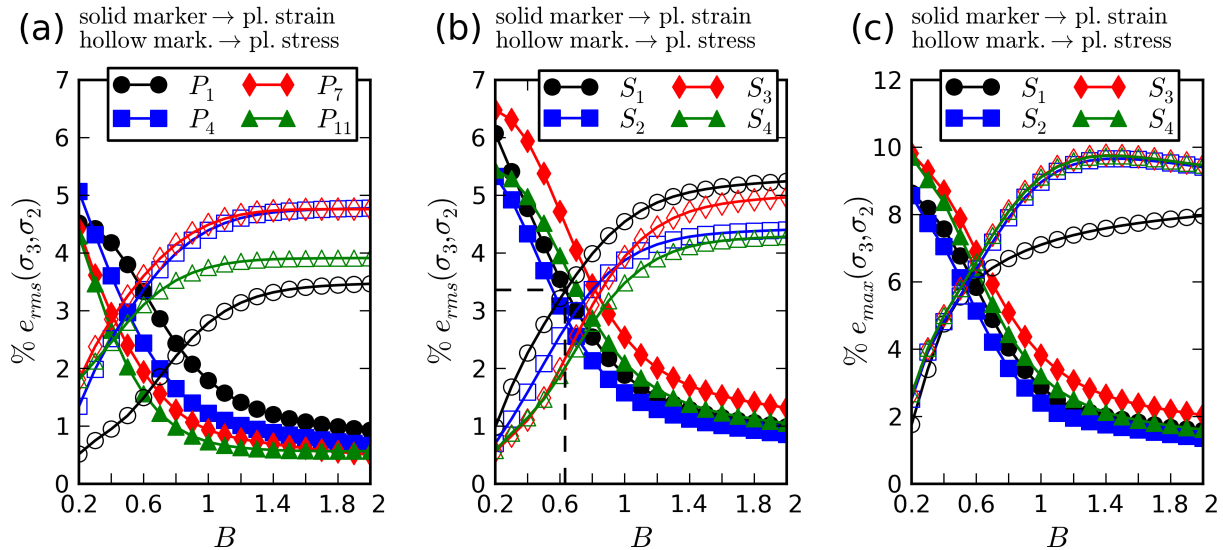


Fig. 6. Error in calculated stresses due to utilizing plane strain (solid markers) and plane stress (hollow markers) assumptions (Eq. 16) as a function of the thickness-normalized width (B) of the actual three-dimensional body: (a) residual stress profile (Legendre) series elements, P_1, P_4, P_7, P_{11} , root-mean-square error; (b,c) residual stress profiles $S_1 \dots S_4$ (Table II), root-mean-square error in part (b) and maximum error in part (c). The intersection point of the plane stress and plane strain curves is shown specifically for profile S_1 in part (b) with dashed lines.

As expected based on Section 3.1, the answer turns out to be dependent on the actual stress profile. For stress series members $P_j, j = 1, \dots, 11$, the transition width ranges between 0.33-0.83 with a tendency to decrease with order. High order profiles like P_{11} are hardly practical residual stress profiles. For the test case stress profiles $S_i, i = 1, \dots, 4$, the transition with values are between 0.63-0.83, likely a more realistic interval.

Fig. 6(c) is the equivalent figure for e_{\max} . To recall, $e_{\max}(\sigma_{2\epsilon}, \sigma_3)$ is the highest error of all $n = 46$ back-calculated stress points given as a percentage of maximum stress magnitude (Equations 13, 15). Through comparison of parts (b) and (c) of Fig. 6, notice that e_{\max} is correlated roughly with a factor of 1.5-2 with e_{rms} . This plot serves to show that individual errors are ‘contained’. The inverse calculations for Fig. 6 assumed the maximum fit order of $m = 11$, however the results in this figure are not sensitive to the fit order provided $m \geq m^*$ for each case.

Since none of the rms errors exceed about 10%, the concern that the inverse solution might amplify the errors appears unfounded. Nonetheless the errors are significant and worthy of correction.

3.4 The effective constraint

This section makes the appropriate definition of the effective constraint (Γ) for this problem and derives it. Γ is the multiplier of the standard pl- ϵ compliance that corresponds to a best approximation of the *stress results* of the 3-D evaluation. To this end, firstly denote the modified compliance with a subscript “ $\Gamma 2\epsilon$ ” as

$$\mathbf{C}_{\Gamma 2\epsilon} = \Gamma \mathbf{C}_{2\epsilon} \quad (23)$$

In contrast to the trivial idea of minimizing of the difference between $\mathbf{C}_3 - \mathbf{C}_{\Gamma 2\epsilon}$ by some metric, matching the *stress results* of the 3-D evaluation means matching the output of the inverse solutions. The following is the form of the inverse solution operator for the modified case obtained by inserting Eq. 23 in Eq. 11:

$$\mathbf{R}_{\Gamma 2\epsilon} = \frac{1}{\Gamma} \mathbf{R}_{2\epsilon} \quad (24)$$

Given strain data ϵ , the difference between the stress results of the two operators is then:

$$\{\sigma_3\} - \{\sigma_{\Gamma 2\epsilon}\} = (\mathbf{R}_3 - \frac{1}{\Gamma} \mathbf{R}_{2\epsilon}) \{\epsilon\} \quad (25)$$

Minimization of $e_{\text{rms}}(\sigma_3, \sigma_{\Gamma 2\epsilon})$ (defined in Eq.14) in terms of Γ , namely, $\frac{\partial}{\partial \Gamma} e_{\text{rms}}(\sigma_3, \sigma_{\Gamma 2\epsilon}) = 0$, yields

$$\Gamma = \frac{\langle \epsilon \rangle \mathbf{R}_{2\epsilon}^T \mathbf{R}_{2\epsilon} \{\epsilon\}}{\langle \epsilon \rangle \mathbf{R}_3^T \mathbf{R}_{2\epsilon} \{\epsilon\}} \quad (26)$$

where $\langle \cdot \rangle$ denotes row vectors. Given this equation, recalling dependencies (Eq. 12), Γ depends on the specific data $\{\epsilon\}$ (alternatively, the specific residual stress), the fit order m , and all the parameters. Taking $\{\epsilon\} = \{\epsilon_3\}$ (Eq. 16) and $\{\epsilon_3\} = \mathbf{C}_3 \{A\}$ (Eq. 9), Eq. 26 can be cast in terms of coefficients:

$$\Gamma = \frac{\langle A \rangle \mathbf{C}_3^T \mathbf{R}_{2\epsilon}^T \mathbf{R}_{2\epsilon} \mathbf{C}_3 \{A\}}{\langle A \rangle \mathbf{P}^T \mathbf{R}_{2\epsilon} \mathbf{C}_3 \{A\}} \quad (27)$$

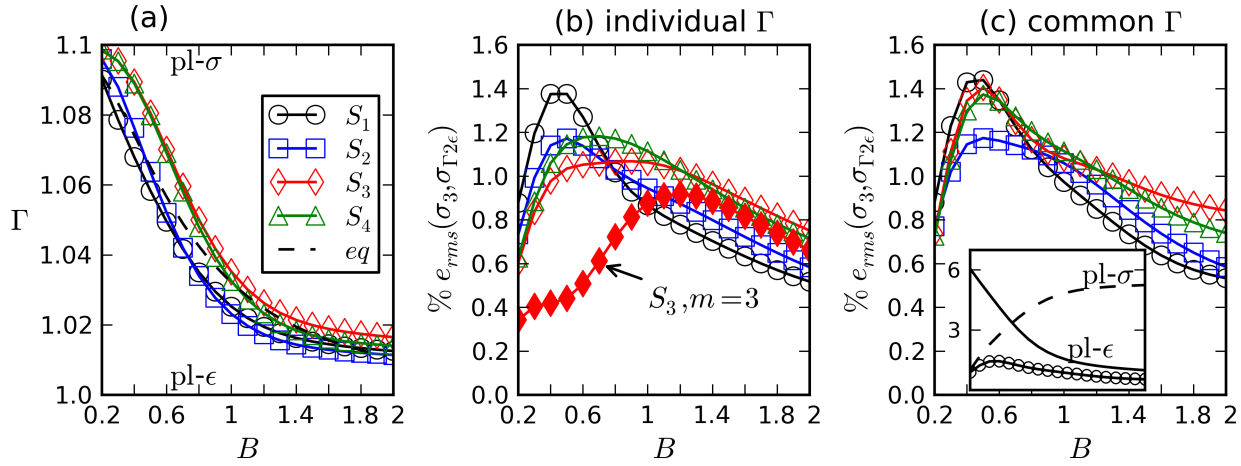


Fig. 7. (a) The effective constraint Γ (Eq. 27) vs. thickness-normalized sample width B for stress profiles $S_1 \cdots S_4$ (Table II) and a representative Lorentzian fit to the combined results labeled *eq*. (b) rms error in each case using the individual Γ corrections in part (a). Fit order is $m = 11$ except the indicated additional curve for S_3 profile with $m = 3$. (c) rms error in each case using the Γ -correction of profile *eq* for all, $m = 11$. Inset: S_1 curve of this plot put in perspective of pl- σ /pl- ϵ errors from Fig. 6.

Γ derived via Eq. 27 for stress profiles $S_1 \cdots S_4$ is plotted in Fig. 7(a) vs. sample width. The plot considers norm values of parameters and full fit order $m = 11$. These Γ -corrections depend on the stress profile as expected; and the remnant rms-error, $e_{rms}(\sigma_3, \sigma_{\Gamma 2\epsilon})$, is plotted in Fig. 7(b). The remnant error makes a peak in the vicinity of $B = 0.6$ for each case. Fig. 5 provides insight in this matter as it shows the level of constraint (γ) variation as a function of slit depth. If there was no variation at all, meaning a flat line, Γ equal to this line's y-intercept would provide a perfect correction with no remnant error. Conversely, as the variation in the constraint level increases, the remnant error increases in the one-parameter Γ -correction which has to negotiate a middle value. The γ -variation is more contained for small widths ($B \sim 0.2$) and large widths (say, $B > 1$) where pl- σ and pl- ϵ dominate the respective cases. Therefore, the remnant error is smaller in these regions than the intermediate widths that exhibit pronounced γ -variation.

To touch on the dependence of the remnant error on the fit order, S_3 is also analyzed with the order of the linear combination itself, namely, $m=m^*=3$, shown in Fig. 7(b). Naturally, two reductions that are equivalent except for fit order m show more discrepancy if the m values are distant. This is why S_3 , with lowest m^* , is picked as a worst case, to reveal maximum discrepancy among its reductions, shown in Fig. 7(b). The $m=11$ reduction reveals more remnant error than the $m=3$ reduction especially for small B , obeying the general trend of higher fit orders enhancing errors in inverse analysis. In principle, then, the $m = 11$ error results of Fig. 7 can be asserted to be worst case.

The practical approach here is to formulate an empirical $\Gamma(B)$ that will have the general characteristic

of the Γ -curves for $S_1 \cdots S_4$ in Fig. 7 (and any other realistic stress profile), that are in fact not so distant from each other. It is also natural to impose $\Gamma(0) = (1 - v^2)^{-1}$, $\Gamma(\infty) = 1$ to a general form to implement the pl- σ and pl- ϵ extremes. Connecting the limiting cases with a Lorentzian-type distribution [dashed lines in Fig 7(a)] and then fitting to the data for $v = 0.3$ yields

$$\Gamma(B) = 1 + \left(\frac{v^2}{1 - v^2}\right) \frac{1}{1 + (B/\Omega)^2} \quad (28)$$

where $\Omega = 0.694$. The remnant errors for correcting with Eq. 28 for all cases are shown in Fig. 7(c). The ultimate justification of the choice and generic use of the Lorentzian form comes from the closeness of the results in parts (b) and (c)—the errors are increased only $\sim 0.2\%$.

The inset in Fig. 7(c) is a visual aid for the user to bring together the results of Figs. 6 and 7. It portrays the error reduction potency of the Γ -correction of Eq. 28 in comparison to merely reducing with 2-D compliances. For clarity, only results for S_1 are shown. Assuming the user knows when to switch from pl- ϵ to pl- σ compliances, the correction's effectiveness is highest around the intersection of pl- ϵ and pl- σ curves reducing the e_{rms} from 3.5% to 1.5%. (Of course, Γ -correction is much bigger if the user is erroneously using pl- ϵ compliances at small widths. The unifying nature of Eq. 28 is significant to avoid such errors as well.) At the norm sample width $B = 1$, the correction is still appreciable reducing e_{rms} from 1.9% to 1%. As expected, reducing with pl- ϵ compliances yield near equivalent results at larger widths. On the other end of the B -spectrum, at $B = 0.2$ note pl- σ reduction is as successful as the Γ -corrected reduction, and it follows that pl- σ compliances can be confidently applied to the unexplored $B < 0.2$. Finally recall, the e_{rms} values of this paragraph have to be multiplied by 1.5-2 to find the maximum individual error e_{max} .

The effective constraint was determined for the studied case of 46 uniform cuts to a depth of 0.92. Since Eq. 26 approximately integrates the pointwise constraints over the range of cut depths, any equally spaced cut depths should return very similar results. Unequal cut depths will weight the results somewhat differently, but the effect is expected to be small for standard experimental usage and similar to the effects of different stress profiles.

3.5 The effect of Poisson's ratio

Because constraint is strongly dependent on Poisson's ratio, and (Eq. 28) was only fit for $v = 0.3$, the procedure of the two prior sections has been repeated for $v = 0.2, 0.25, 0.35, 0.4$. A representative

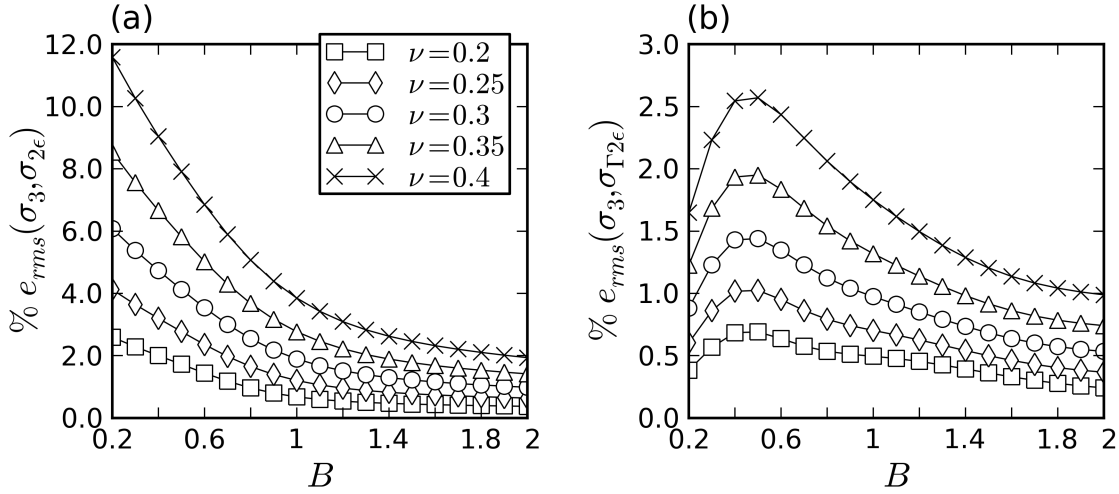


Fig. 8. For Poisson's ratios 0.2, ..., 0.4, plots of (a) rms-error in reducing profile S_1 with plane strain compliances, (b) remnant rms-error after one-parameter correction with Eq. 28, versus thickness-normalized sample width B .

part of the plots is regenerated for different Poisson's ratios in Fig. 8. The attention is constrained to stress profile S_1 and part (a) shows rms-errors upon plane strain reduction, $e_{\text{rms}}(\sigma_{2\epsilon}, \sigma_3)$, a la Fig. 6(b). The errors, as expected, increase with higher Poisson's ratio. This tendency is also valid for remnant errors plotted in part (b) a la Fig. 7(c). The Γ -correction here is Eq. 28 that was fit with only $\nu = 0.3$ data. Using this form only reduces complexity, noting that individual Γ -corrections for each ν (not shown) yield hardly smaller remnant errors. The strong dependence on Poisson's ratio is illustrated by the scaling factor $\nu^2/1 - \nu^2$, which is 0.042, 0.099, 0.190 for $\nu = 0.2, 0.3, 0.4$, respectively. The error curves in Fig. 8 scale with $\nu^2/1 - \nu^2$ substantially in part (a) and more approximately in part (b). Hence errors for materials with $\nu > 0.33$ (aluminum, brass, copper, zinc, titanium, magnesium), errors would be about 25% greater than those for $\nu = 0.3$ and for materials with ν close to 0.4 (gold, some nickel alloys) or even greater (lead, polymers) the errors would be double or more those for $\nu = 0.3$.

It should not, however, be understood that this result stems from a trivial proportional relation between compliances of different ν . In fact, the ratio of Green's functions of different Poisson's ratio (otherwise equivalent) samples, $G_3(x, a, \nu_1, \dots)/G_3(x, a, \nu_2, \dots)$, in general, shows pronounced variation with (x, a) [not shown].

3.6 The effect of gage width

The gage width error proves to be worst for smallest width, $B = 0.2$. The largest gage width considered $l_z = 0.2$ (about 3 times the chosen gage length), covers the entire sample width at this point. Even then, the error $e_{\text{rms}}(\sigma_3(l_z = 0.2), \sigma_3(l_z = 0))$ stays below 0.25%. This means the gage width error can effectively be disregarded.

4 Conclusions

This manuscript investigated the effects of analyzing a 3-D body with a 2-D model in the slitting method for measuring residual stresses in the rectangular bar geometry. A simple one-parameter correction provides the effective 3-D constraint and greatly reduces the errors from using 2-D compliances, which are still used by the vast majority of practitioners. Furthermore, the result is crucial for making an accurate standard for the slitting method because only 2-D compliances can be compactly tabulated.

The correction procedure can be briefly summarized as follows. One starts with $p1-\epsilon$ compliances from a custom 2-D finite element analysis or from available compilations [9]. If necessary, compliances are scaled to the appropriate elastic constants using Eq. 4. The effective constraint Γ for the given Poisson's ratio and specimen width (normalized by thickness) is calculated from Eq. 28. The corrected compliances are calculated by simple multiplication in Eq. 23 and then used to calculate stresses with the standard procedure presented in Section 2.3.

Without any correction, the worst root-mean-square (rms) error in the calculated stress profile from using 2-D compliances is about 7% for the case of $\nu = 0.3$. Maximum errors are about twice the rms errors. Using the optimal 2-D compliances, $p1-\sigma$ for $B < 0.7$ and $p1-\epsilon$ otherwise, reduces the rms errors to about 3.5%. Using the effective constraint correction further reduced the worst rms error to about 1.5%, as shown in Fig. 7(c). For Poisson's ratio dependence, the study asserts that errors roughly proportional to $\nu^2/1 - \nu^2$. This will mean, e.g., $\nu = 0.4$ errors are a factor of 1.92 higher than $\nu = 0.3$ errors, which are reviewed in detail above.

For width $B = 1$, the remnant rms-error is reduced to under 1%, and does not drop too much further with increasing B . Considering experimental difficulties with testing overly wide samples, it is more than possible to include more error while trying to make an incremental error reduction based on the assumptions of this work. As a compromise, if the user is at the liberty of choosing a sample width, $B \sim 1 - 1.5$ is recommended.

Acknowledgements

This work was supported by B.U. Research Fund at Bogazici University under contract 09A605P. The authors would like to thank members of ASTM Task Group E28.13.02 for helpful discussions. Some of this work was performed at Los Alamos National Laboratory, operated by the Los Alamos National Security, LLC for the National Nuclear Security Administration of the U.S. Department of Energy under contract DE-AC52-06NA25396. By acceptance of this article, the publisher recognizes that the U.S. Government retains a nonexclusive, royalty-free license to publish or reproduce the published

form of this contribution, or to allow others to do so, for U.S. Government purposes.

References

- [1] Cheng, W., and Finnie, I., 2007. *Residual stress measurement and the slitting method*. Springer, New York.
- [2] Aydiner, C. C., Ustundag, E., Prime, M. B., and Peker, A., 2003. “Modeling and measurement of residual stresses in a bulk metallic glass plate”. *J Non-Cryst Solids*, **316**(1), pp. 82–95.
- [3] Kim, B.-S., Bernet, N., Sunderland, P., and Manson, J.-A., 2002. “Numerical analysis of the dimensional stability of thermoplastic composites using a thermoviscoelastic approach”. *J Compos Mater*, **36**(20), pp. 2389–2403.
- [4] Ersoy, N., and Vardar, O., 2000. “Measurement of residual stresses in layered composites by compliance method”. *J Compos Mater*, **34**(7), pp. 575–598.
- [5] Prime, M. B., and Hill, M. R., 2004. “Measurement of fiber-scale residual stress variation in a metal-matrix composite”. *J Compos Mater*, **38**(23), pp. 2079–95.
- [6] Sabaté, N., Vogel, D., Gollhardt, A., Keller, J., Cané, C., Grácia, I., Morante, J., and Michel, B., 2006. “Measurement of residual stress by slot milling with focused ion-beam equipment”. *J Micromech Microeng*, **16**(2), pp. 254–259.
- [7] Aydiner, C., and Üstündag, E., 2005. “Residual stresses in a bulk metallic glass cylinder induced by thermal tempering”. *Mech Mater*, **37**(1), pp. 201–212.
- [8] Prime, M. B., and Hill, M. R., 2006. “Uncertainty, model error, and order selection for series-expanded, residual-stress inverse solutions”. *J Eng Mater-T ASME*, **128**(2), pp. 175–85.
- [9] Lee, M. J., and Hill, M. R., 2007. “Effect of strain gage length when determining residual stress by slitting”. *J Eng Mater-T ASME*, **129**(1), pp. 143–150.
- [10] Prime, M. B., 2010. “Plasticity effects in incremental slitting measurement of residual stresses”. *Eng Fract Mech*, **77**(10), pp. 1552–1566.
- [11] Cheng, W., and Finnie, I., 1997. “Computation of mode I stress intensity factors for three-dimensional bodies using displacements at an arbitrary location”. *Int J Fracture*, **83**(1), pp. 91–104.
- [12] Nervi, S., and Szabó, B., 2007. “On the estimation of residual stresses by the crack compliance method”. *Comput Method Appl M*, **196**(37-40 SPEC. ISS.), pp. 3577–3584.
- [13] Fratini, L., and Pasta, S., 2010. “On the residual stresses in friction stir-welded parts: effect of the geometry of the joints”. *Proceedings of the Institution of Mechanical Engineers, Part L: Journal of Materials Design and Applications*, **224**(4), pp. 149–161.

- [14] Schindler, H. J., 2000. “Residual stress measurement in cracked components: capabilities and limitations of the cut compliance method”. *Materials Science Forum*, **347-349**, pp. 150–155.
- [15] Bueckner, H. F., 1958. “The propagation of cracks and the energy of elastic deformation”. *Trans. Am. Soc. Mech. Eng.*, **80**, pp. 1225–1230.
- [16] Schajer, G. S., and Prime, M. B., 2006. “Use of inverse solutions for residual stress measurements”. *J Eng Mater-T ASME*, **128**(3), pp. 375–82.
- [17] Abaqus FEA, D S Simulia, ©Dassault Systemés 2004, 2010.
- [18] Lutz, M., 2009. *Learning Python*, 4 ed. O’Reilly Media.
- [19] Jones, E., Oliphant, T., Peterson, P., et al., 2001–. SciPy: Open source scientific tools for Python.
- [20] Parsons, I. D., Hall, J. F., and Rosakis, A., 1987. “A finite element investigation of the elastostatic state near a three dimensional edge crack”. In 20th Midwestern Mechanics Conference, Vol. 14b, pp. 729–734.
- [21] Nakamura, T., and Parks, D. M., 1989. “Antisymmetrical 3-d stress-field near the crack front of a thin elastic plate”. *International Journal of Solids and Structures*, **25**(12), pp. 1411–1426.
- [22] Subramanya, H. Y., Viswanath, S., and Narasimhan, R., 2005. “A three-dimensional numerical study of mixed mode (i and ii) crack tip fields in elastic-plastic solids”. *International Journal of Fracture*, **136**(1-4), pp. 167–185.
- [23] Khan, S. M. A., 2012. “Effect of the thickness on the mixed mode crack front fields”. *Structural Engineering and Mechanics*, **42**(5), pp. 701–713.
- [24] Cheng, W., Finnie, I., and Vardar, O., 1992. “Deformation of an edge-cracked strip subjected to normal surface traction on the crack faces”. *Eng Fract Mech*, **42**(1), pp. 97–107.
- [25] Schindler, H. J., Cheng, W., and Finnie, I., 1997. “Experimental determination of stress intensity factors due to residual stresses”. *Exp Mech*, **37**(3), pp. 272–7.

List of Figure Captions

Figure 1. The (a) 2-D and (b) 3-D finite element domains of the slitting sample depicted as shaded regions in the top sketches of the entire sample. O is the origin of the chosen x - y - z coordinate system; SG stands for strain gage; δ is a point/line load in (a)/(b).

Figure 2. (a) The first four elements of the stress series (Legendre polynomials 2 to 5), (b) the considered residual stress profiles detailed in Table II.

Figure 3. A considered 3-D finite element mesh composed of wedge and hexahedron elements. All parameters are at norm values ($B = 1$, $L = 4$, $w = 0$) and the shown slit depth, a , is arbitrary. O is the origin (refer to Fig. 1(b) for notation) and the front face is placed in a rectangle also revealing the corresponding 2-D mesh. The x - y - z triad is displaced from O for clarity.

Figure 4. For $B = 1$ and $\nu = 0.3$, constraint ratios (Eq. 19) of (a) strain at the gage, (b) depth-derivative of the strain at the gage, and (c) energy release rate. Each curve in parts (a), (b) or (c) corresponds to fixing the δ -load (see Fig. 1) at the x value shown in the legend and plots the corresponding ratio as a function slit depth a . The pl- σ level is at $(1 - \nu^2)^{-1} = 1.099$.

Figure 5. The ratio of the measured strain, γ , in the 3-D analysis to plane strain analysis as a function of slit depth a . The particular loading is a δ -load (see Fig. 1) at the top ($x = 0$). This figure is at the norm point of the parameter space $\nu = 0.3$, etc., except for each curve corresponding to different sample widths as indicated.

Figure 6. Error in calculated stresses due to utilizing plane strain (solid markers) and plane stress (hollow markers) assumptions (Eq. 16) as a function of the thickness-normalized width (B) of the actual three-dimensional body: (a) residual stress profile (Legendre) series elements, P_1, P_4, P_7, P_{11} , root-mean-square error; (b,c) residual stress profiles $S_1 \cdots S_4$ (Table II), root-mean-square error in part (b) and maximum error in part (c). The intersection point of the plane stress and plane strain curves is shown specifically for profile S_1 in part (b) with dashed lines.

Figure 7. (a) The effective constraint Γ (Eq. 27) vs. thickness-normalized sample width B for stress profiles $S_1 \cdots S_4$ (Table II) and a representative Lorentzian fit to the combined results labeled eq . (b) rms error in each case using the individual Γ corrections in part (a). Fit order is $m = 11$ except the indicated additional curve for S_3 profile with $m = 3$. (c) rms error in each case using the Γ -correction of profile eq for all, $m = 11$. Inset: S_1 curve of this plot put in perspective of pl- σ /pl- ϵ errors from Fig. 6.

Figure 8. For Poisson's ratios 0.2, ..., 0.4, plots of (a) rms-error in reducing profile S_1 with plane strain compliances, (b) remnant rms-error after one-parameter correction with Eq. 28, versus thickness-normalized sample width B .

List of Table Captions

Table I. Parameters (\mathbf{p}_3) of the study (column 1), their norm values (column 2), and considered values/ranges of the parametric study (column 3).

Table II. Considered residual stress profiles, their typical causes, Legendre series order (m^*) and coefficients (A_i).